High-precision analysis of the critical point in heavy-quark QCD at $N_t = 6$

Ryo Ashikawa,[1] Masakiyo Kitazawa[2,3,*] Shinji Ejiri,[4] and Kazuyuki Kanaya[5]

[1]*Department of Physics, Osaka University, Toyonaka, Osaka 560-0043, Japan*

[2]*Yukawa Institute for Theoretical Physics, Kyoto University, Kyoto, 606-8502, Japan*

[3]*J-PARC Branch, KEK Theory Center, Institute of Particle and Nuclear Studies,
KEK, Tokai, Ibaraki 319-1106, Japan*

[4]*Department of Physics, Niigata University, Niigata 950-2181, Japan*

[5]*Tomonaga Center for the History of the Universe, University of Tsukuba,
Tsukuba, Ibaraki 305-8571, Japan*

Binder-cumulant analysis of the critical point in the heavy-quark region of QCD is performed by Monte-Carlo simulations with the hopping-parameter expansion at $N_t = 6$. We extend our previous analysis at $N_t = 4$ to finer lattices and perform high-precision analyses on large spatial volumes up to the aspect ratio $LT = N_s/N_t = 18$. Higher order terms in the hopping-parameter expansion are incorporated effectively up to 14th order. The numerical results show that the violation of the finite-size scaling becomes more prominent on the finer lattice at a given aspect ratio.

I. INTRODUCTION

Appearance of critical points (CPs) in quantum chromodynamics (QCD) in medium with variations of various external parameters is one of the interesting features of this theory. CPs are expected to exist on the phase diagram of QCD on the temperature and baryon chemical potential plane at physical quark masses [1,2]. These CPs are the main targets of the beam-energy scan program in relativistic heavy-ion collisions [3–6]. Although their search in lattice-QCD numerical simulations is difficult due to the sign problem, various attempts to approach the CP are ongoing [7–18]. CPs are also expected to manifest themselves at vanishing baryon chemical potential when the quark masses are varied from the physical ones both toward the light and heavy directions, as nicely summarized on the so-called Columbia plot [19,20]. Even other CPs may manifest themselves provoked by spatial boundary conditions [21].

The CPs in the light and heavy quark-mass regions have been investigated in lattice-QCD numerical simulations for decades [12,22–32]. Since they appear at zero baryon chemical potential, these analyses can be carried out without suffering from the sign problem. For the CP in

*Contact author: kitazawa@yukawa.kyoto-u.ac.jp

the light-quark region, however, recent analyses give controversial results and even the existence of the CP off the chiral limit is not clear [12,20,29]. While the existence of the CP is robust for the heavy-quark region, a proper reproduction of the expected scaling behavior from the $Z(2)$ universality class, to which the CP is believed to belong, is known to be difficult [30,31].

The Binder-cumulant analysis [33] is one of the useful methods that have been used in these studies. Using the finite-size scaling (FSS) of the scaling function, this method allows us to reveal various properties of the CP in the thermodynamic limit, such as the location and critical exponents, from the numerical results for finite-volume systems. In the Binder-cumulant analysis, however, it is usually assumed that the thermodynamics is dominated by the "singular part" that obeys the scaling behavior. This assumption, however, is justified only in the vicinity of the CP and for sufficiently large spatial volumes. In practical numerical simulations that are performed on finite volumes, the numerical results are always contaminated by the "nonsingular part" that violates the ideal FSS behavior. The controversial situations in the analyses both in the light and heavy quark-mass regions may stem from the nonsingular part that is not suppressed well at the spatial volumes used in the simulations.

In Ref. [31], motivated by this observation, part of the authors of the present paper have performed the Binder-cumulant analysis around the CP in the heavy-quark region of QCD on large spatial volumes. The aspect ratio is taken up to $LT = N_s/N_t = 12$, with $L = N_s a$ the spatial lattice size and $T = 1/(N_t a)$ the temperature, while the lattice

spacing a was fixed to a coarse one with the temporal lattice extent $N_t = 4$. To realize the large-volume simulations, the hopping-parameter expansion (HPE) for the quark determinant was employed: Monte-Carlo simulations are performed at the leading nontrivial order (LO) of the HPE, and the next-to-leading-order (NLO) contributions are taken into account by reweighting. It has been shown that the truncation error of the HPE is well suppressed around the CP at $N_t = 4$ in this analysis, and also this method enables efficient numerical analysis there. Through the Binder-cumulant analysis using the precision numerical results on large lattices, it was found that the violation of the FSS is not negligible even at $LT = 8$ for $N_t = 4$.

In the present study, we extend this analysis to a finer lattice with $N_t = 6$. To see the correct scaling behavior, we also enlarge the aspect ratio up to $LT = 18$. Besides the prescription to deal with the HPE up to NLO used in Ref. [31], we newly employ a method proposed in Ref. [34] to incorporate higher order terms in the HPE effectively into the analysis. Although the convergence of the HPE becomes worse as the continuum limit is approached, this method allows us to incorporate virtually all orders in the HPE near the CP at $N_t = 6$. These numerical results enable us to fix the location of the CP with high precision. It will also be shown that the violation of the FSS becomes more prominent at $N_t = 6$ compared to the coarse-lattice simulations in Ref. [31].

This paper is organized as follows. In the next section, we describe the lattice action and its HPE, and the procedure to deal with the higher-order terms of the HPE in the numerical analysis. In Sec. III, we discuss the detailed setup and parameters of our Monte-Carlo simulations. The numerical results are then presented in Sec. IV. The last section is devoted to a short summary. The convergence of the HPE is discussed in Appendix.

II. HOPPING-PARAMETER EXPANSION

In this section, we summarize the HPE and a method to handle the effects of its higher-order terms.

A. Lattice action

Our lattice QCD action is decomposed as $S = S_g + S_q$ with the gauge and quark actions S_g and S_q. We employ the Wilson gauge action

$$S_g = -6N_{\text{site}}\beta\hat{P}, \qquad (1)$$

with the space-time lattice volume $N_{\text{site}} = N_s^3 \times N_t$, the gauge coupling parameter $\beta = 6/g^2$, and the plaquette operator

$$\hat{P} = \frac{1}{6N_c N_{\text{site}}}\sum_{x,\mu<\nu}\text{Re}\,\text{tr}_C[U_{x,\mu}U_{x+\hat{\mu},\nu}U^\dagger_{x+\hat{\nu},\mu}U^\dagger_{x,\nu}], \quad (2)$$

where $U_{x,\mu}$ is the link variable in the μ direction at site x, tr_C is the trace over color indices, and $N_c = 3$. For S_q, we employ the Wilson quark action

$$S_q = \sum_{f=1}^{N_f}\sum_{x,y}\bar{\psi}_x^{(f)}M_{xy}(\kappa_f)\psi_y^{(f)}, \qquad (3)$$

with the Wilson quark kernel

$$M_{xy}(\kappa) = \delta_{xy} - \kappa B_{xy}, \qquad (4)$$

$$B_{xy} = \sum_{\mu=1}^{4}[(1-\gamma_\mu)U_{x,\mu}\delta_{y,x+\hat{\mu}} + (1+\gamma_\mu)U^\dagger_{y,\mu}\delta_{y,x-\hat{\mu}}], \quad (5)$$

where the color and Dirac-spinor indices are suppressed for simplicity. κ_f is the hopping parameter for the fth flavor, which is related to the bare quark mass m_f as $\kappa_f = 1/(2m_f a + 8)$. In the following, we consider the case of degenerated N_f flavors with a common hopping parameter $\kappa = \kappa_f$, whereas generalization to nondegenerate cases is straightforward.

After integrating out the quark degrees of freedom, the expectation value of a gauge operator $\hat{O}(U)$ is given by

$$\langle\hat{O}(U)\rangle = \frac{1}{Z}\int\mathcal{D}U\,\hat{O}(U)e^{-S_{\text{eff}}}, \qquad (6)$$

with

$$S_{\text{eff}} = S_g - N_f\ln\det M(\kappa), \qquad (7)$$

and the partition function $Z = \int\mathcal{D}U\,e^{-S_{\text{eff}}}$.

B. Hopping-parameter expansion

In the heavy-quark region $\kappa \ll 1$, $\ln\det M$ in Eq. (7) is expanded with respect to κ at $\kappa = 0$ as

$$\ln\left[\frac{\det M(\kappa)}{\det M(0)}\right] = -\sum_{n=1}^{\infty}\frac{1}{n}\text{Tr}[B^n]\kappa^n. \qquad (8)$$

Here, Tr is the trace over all indices and an irrelevant contribution at $\kappa = 0$ is subtracted in Eq. (8). The nth-order terms in the HPE are graphically represented by the closed trajectories of length n [31,35].

On gauge configurations at nonzero temperature with the temporal extent N_t, the HPE of S_{eff} is written as

$$S_{\text{eff}} = S_g - N_f N_{\text{site}}\sum_{n=1}^{\infty}(\hat{W}(n) + \hat{L}(N_t, n))\kappa^n, \quad (9)$$

where $\hat{W}(n)$ and $\hat{L}(N_t, n)$ are contributions from trajectories without and with windings along the temporal direction, provided that the spatial extent is sufficiently large such that the spatial windings are negligible. We refer to the terms included in the former and the latter as the Wilson

loops and the Polyakov-loop-type (PLT) loops, respectively. We set $\hat{W}(n) = \hat{L}(N_t, n) = 0$ if corresponding closed loops of length n do not exist, e.g. $\hat{W}(n) = 0$ for $n < 4$ or odd n, and $\hat{L}(N_t, n) = 0$ for $n < N_t$.

The LO contributions from the Wilson and PLT loops are calculated to be

$$\hat{W}(4) = W_0(4)\hat{P}, \tag{10}$$

$$\hat{L}(N_t, N_t) = L_0(N_t, N_t)\mathrm{Re}\hat{\Omega}, \tag{11}$$

with the Polyakov loop

$$\hat{\Omega} = \frac{1}{N_c N_s^3}\sum_{\vec{x}}\mathrm{tr}_C[U_{\vec{x},4}U_{\vec{x}+\hat{4},4}U_{\vec{x}+2\cdot\hat{4},4}\cdots U_{\vec{x}+(N_t-1)\cdot\hat{4},4}], \tag{12}$$

where $W_0(n)$ and $L_0(N_t, n)$ are the values of $\hat{W}(n)$ and $\hat{L}(N_t, n)$ in the weak-coupling limit, respectively, which is obtained by setting $U_{x,\mu} = 1$ for all link variables [34]. The calculation of $W_0(n)$ and $L_0(N_t, n)$ is given in Appendix. For the LO we obtain

$$W_0(4) = 96N_c, \qquad L_0(N_t, N_t) = \frac{2^{N_t+2}N_c}{N_t}. \tag{13}$$

The NLO terms are calculated to be

$$\hat{W}(6) = W_0(6)\hat{P}_6, \tag{14}$$

$$\hat{L}(N_t, N_t + 2) = L_0(N_t, N_t + 2)\mathrm{Re}\hat{\Omega}_{N_t+2}, \tag{15}$$

with $W_0(6) = 2816N_c$ and

$$\hat{P}_6 = \frac{1}{11}(3\hat{W}_{\mathrm{rec}} + 6\hat{W}_{\mathrm{chair}} + 2\hat{W}_{\mathrm{crown}}), \tag{16}$$

where $\hat{W}_{\mathrm{rec}}$, $\hat{W}_{\mathrm{chair}}$, and $\hat{W}_{\mathrm{crown}}$ represent the six-step Wilson loops of the rectangular, chair, and crown types, respectively. The $\hat{\Omega}_{N_t+2}$ in Eq. (15) is the summation of bent PLT loops of length $N_t + 2$. Definitions of these operators, as well as the derivation of these results, are found in Refs. [31,34]. Note that all the Wilson and PLT loops are normalized such that $\hat{P} = \hat{P}_6 = \hat{W}_{\mathrm{rec}} = \hat{W}_{\mathrm{chair}} = \hat{W}_{\mathrm{crown}} = 1$ and $\hat{\Omega} = \hat{\Omega}_{N_t+2} = 1$ in the weak-coupling limit.

We rewrite the expansion (9) as

$$S_{\mathrm{eff}} = S_g + S_{\mathrm{LO}} + S_{\mathrm{NLO}} + \cdots, \tag{17}$$

where S_{LO} and S_{NLO}, respectively, contain the LO and NLO contributions from the Wilson and PLT loops as

$$S_{\mathrm{LO}} = -N_f N_{\mathrm{site}}(\hat{W}(4)\kappa^4 + \hat{L}(N_t, N_t)\kappa^{N_t}), \tag{18}$$

$$S_{\mathrm{NLO}} = -N_f N_{\mathrm{site}}(\hat{W}(6)\kappa^6 + \hat{L}(N_t, N_t + 2)\kappa^{N_t+2}). \tag{19}$$

The action at the LO is given by

$$\begin{aligned}S_{g+\mathrm{LO}} &= S_g + S_{\mathrm{LO}}\\ &= -6N_{\mathrm{site}}\beta^*\hat{P} - \lambda N_s^3\mathrm{Re}\hat{\Omega},\end{aligned} \tag{20}$$

with

$$\beta^* = \beta + \frac{N_f W_0(4)}{6}\kappa^4 = \beta + 16N_f N_c\kappa^4, \tag{21}$$

$$\lambda = N_f N_t L_0(N_t, N_t)\kappa^{N_t} = 2^{N_t+2}N_f N_c\kappa^{N_t}. \tag{22}$$

As shown in Ref. [31], we can adopt a pseudo-heat-bath algorithm for the Monte-Carlo simulation of $S_{g+\mathrm{LO}}$ with a numerical cost comparable to that of the pure gauge theory S_g, i.e., with a cost much lower than that of the full QCD. This enables us to carry out simulations on lattices with large spatial volumes.

C. Effective incorporation of higher order terms

In Ref. [34], a method to effectively incorporate the NNLO and yet higher order terms into numerical analyses has been proposed. The key ingredient of the method is that $\hat{W}(n)$ and $\hat{L}(N_t, n)$ at different n, respectively, are strongly correlated with one another such that the approximate relations

$$\frac{\hat{W}(n)}{W_0(n)} \simeq d_n \frac{\hat{W}(4)}{W_0(4)} + f_n = d_n\hat{P} + f_n, \tag{23}$$

$$\frac{\hat{L}(N_t, n)}{L_0(N_t, n)} \simeq c_n \frac{\hat{L}(N_t, N_t)}{L_0(N_t, N_t)} = c_n\mathrm{Re}\hat{\Omega}, \tag{24}$$

hold well configuration by configuration, where d_n, f_n, and c_n are parameters common to all configurations. In Ref. [34], the validities of Eqs. (23) and (24) have been investigated on pure gauge configurations, i.e. in the heavy quark limit. It was found that Eq. (24) is well applicable up to very high n. Although the correlations among the Wilson loops turned out to be weaker than the PLT loops, Eq. (23) is also found to be well justified for small n. We will show later that the same tendency is also obtained on the gauge configurations generated by $S_{g+\mathrm{LO}}$ around the CP in the heavy-quark region.

Once one accepts Eqs. (23) and (24) as equalities, one can rewrite the action including the Wilson and PLT loops up to n_{W}th and n_{L}th orders, respectively,

$$S^{(n_{\mathrm{W}},n_{\mathrm{L}})} = S_g - N_f N_{\mathrm{site}}\left(\sum_{n=4}^{n_{\mathrm{W}}}\hat{W}(n)\kappa^n + \sum_{n=N_t}^{n_{\mathrm{L}}}\hat{L}(N_t, n)\kappa^n\right), \tag{25}$$

as

$$S^{(n_{\mathrm{W}},n_{\mathrm{L}})} \simeq S_{\mathrm{eff}[\mathrm{LO}]}^{(n_{\mathrm{W}},n_{\mathrm{L}})} = -6N_{\mathrm{site}}\beta_{n_{\mathrm{W}}}^*\hat{P} - \lambda_{n_{\mathrm{L}}}^*N_s^3\mathrm{Re}\hat{\Omega}, \tag{26}$$

with

$$\beta^*_{n_{\rm W}} = \beta + \frac{N_{\rm f}}{6}\sum_{n=4}^{n_{\rm W}} d_n W_0(n)\kappa^n, \qquad (27)$$

$$\lambda^*_{n_{\rm L}} = N_{\rm f}N_t \sum_{n=N_t}^{n_{\rm L}} c_n L_0(N_t, n)\kappa^n, \qquad (28)$$

up to an irrelevant constant. The fact that Eq. (26) has the same form as Eq. (20) with the replacements $\beta^* \to \beta^*_{n_{\rm W}}$ and $\lambda \to \lambda^*_{n_{\rm L}}$ means that the numerical results at the LO can be reinterpreted as those for the action $S^{(n_{\rm W}, n_{\rm L})}$ with a simple replacement of the simulation parameters. The measurements of higher order terms in the HPE are not necessary in this analysis once d_n and c_n are determined numerically.

This interpretation, however, relies on Eqs. (23) and (24), which become less reliable for larger n. This problem can be partially resolved if one measures the NLO terms, $\hat{W}(6)$ and $\hat{L}(N_t, N_t + 2)$, on every configuration. Since the correlations of $\hat{W}(n)$ or $\hat{L}(N_t, n)$ between different n are stronger for closer n, it is better to approximate higher order terms as

$$\frac{\hat{W}(n)}{W_0(n)} \simeq \tilde{d}_n \frac{\hat{W}(6)}{W_0(6)} + \tilde{f}_n = \tilde{d}_n \hat{P}_6 + \tilde{f}_n, \qquad (29)$$

$$\frac{\hat{L}(N_t, n)}{L_0(N_t, n)} \simeq \tilde{c}_n \frac{\hat{L}(N_t, N_t + 2)}{L_0(N_t, N_t + 2)} = \tilde{c}_n {\rm Re}\hat{\Omega}_{N_t+2}, \qquad (30)$$

for $n \geq 8$ and $n \geq N_t + 4$, respectively, than Eqs. (23) and (24). Assuming Eqs. (29) and (30) as equalities, one obtains an approximate action of $S^{(n_{\rm W}, n_{\rm L})}$ as

$$S^{(n_{\rm W}, n_{\rm L})}_{\rm eff[NLO]} = S_{\rm g+LO} - N_{\rm site}(\gamma_{n_{\rm W}}\hat{P}_6 + \xi_{n_{\rm L}}{\rm Re}\hat{\Omega}_{N_t+2}), \qquad (31)$$

with

$$\gamma_{n_{\rm W}} = N_{\rm f}\sum_{n=6}^{n_{\rm W}} \tilde{d}_n W_0(n)\kappa^n, \qquad (32)$$

$$\xi_{n_{\rm L}} = N_{\rm f}\sum_{n=N_t+2}^{n_{\rm L}} \tilde{c}_n L_0(N_t, n)\kappa^n. \qquad (33)$$

In later sections, we use Eq. (31) for the numerical analyses by performing Monte-Carlo simulations with $S_{\rm g+LO}$ and taking the effects of the second term by reweighting. A comparison with the method using Eq. (26), as well as the analysis at NLO, is given in Appendix A 2.

D. Numerical study of higher order terms

Now, let us investigate the validity of the above approximate formulas for the action numerically. For this purpose we generate 100 gauge configurations for the action S_{g+LO} with $N_{\rm f} = 2$ on the $36^3 \times 6$ lattice at the parameters close to
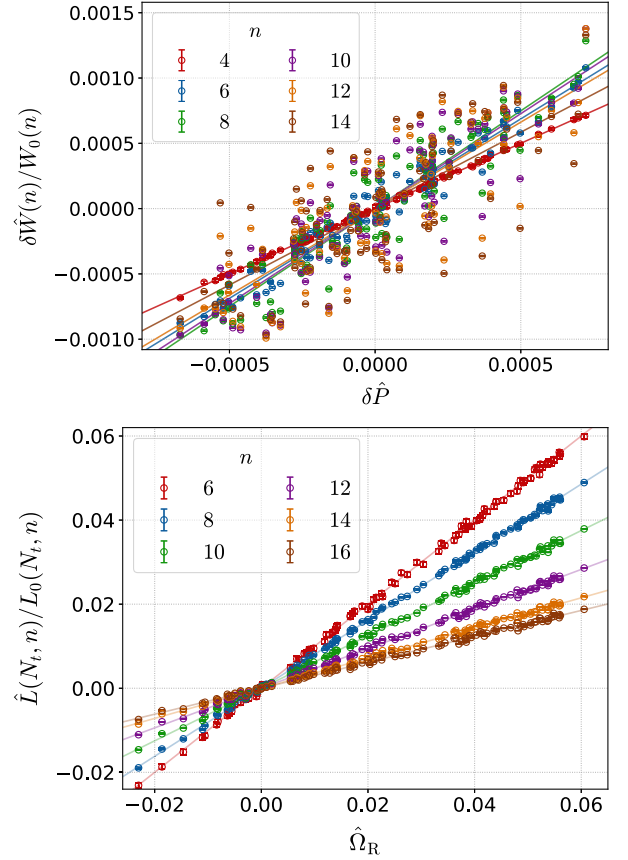

FIG. 1. Scatter plots of $(\delta\hat{W}(n)/W_0(n), \delta\hat{P})$ and $(\hat{L}(N_t, n)/L_0(N_t, n), \hat{\Omega}_{\rm R})$ on 100 gauge configurations of the size $N_s^3 \times N_t = 36^3 \times 6$ near the CP for various values of n. The lines show the results of the linear fits with Eqs. (23) and (24) for each n.

the CP at the LO, $(\beta^*, \lambda) = (5.8905, 0.0012)$. We measure $\hat{W}(n)$ and $\hat{L}(N_t, n)$ on each configuration through the measurement of B^n by the noise method [34] with 5,000 noise vectors.

In Fig. 1, we show the scatter plots of $(\delta\hat{W}(n)/W_0(n), \hat{P})$ and $(\hat{L}(N_t, n)/L_0(N_t, n), \hat{\Omega}_{\rm R} = {\rm Re}\hat{\Omega})$ measured on every configuration for various n with $\delta\hat{W}(n) = \hat{W}(n) - \langle\hat{W}(n)\rangle$. The figure shows that each result distributes linearly, indicating the strong correlations (23) and (24), whereas the distribution tends to be more scattered as n becomes larger, especially in $\hat{W}(n)$.

The coefficients d_n, c_n, $\tilde{d}_n$, and $\tilde{c}_n$ determined from these results by the linear fits are summarized in Table I, where the statistical errors are estimated by the jackknife method. The errors from the noise method are well suppressed compared to the statistical ones.[1] The results of d_n and c_n

---

[1]As discussed in Ref. [34], concerning c_n and $\tilde{c}_n$ in Table I, the cases $n = 18$ and 20 for $N_t = 6$ are special because the sign of $L_0(N_t, n)$ changes between $n = 18$ and 20 and thus $L_0(N_t, n)$ suffers from strong cancellation of positive and negative terms at $n = 18$ and 20. For $N_t = 8$, this happens first between $n = 26$ and 28.

TABLE I. Values of d_n, c_n, $\tilde{d}_n$, and $\tilde{c}_n$ obtained on the $36^3 \times 6$ lattice with S_{g+LO} near the CP at $N_f = 2$. The errors are the statistical ones.

n	d_n	$\tilde{d}_n$
4	1	
6	1.374(24)	1
8	1.498(52)	1.126(21)
10	1.454(76)	1.120(40)
12	1.324(96)	1.041(56)
14	1.17(11)	0.938(68)
16	1.03(13)	0.845(79)
18	0.96(14)	0.797(93)
20	1.02(18)	0.86(12)

n	c_n	$\tilde{c}_n$
6	1	
8	0.8091(14)	1
10	0.6251(16)	0.7727(9)
12	0.4710(15)	0.5822(12)
14	0.3585(13)	0.4430(12)
16	0.3084(14)	0.3808(16)
18	1.0074(67)	1.2419(91)
20	−0.02730(6)	−0.0334(9)
22	0.0088(3)	0.01083(3)

are close to those obtained on pure gauge simulations [34], suggesting a mild dependence of d_n and c_n on λ and β^* near

the phase transition. We thus employ the values given in Table I in the following analyses.

To see the correlations in more detail, in Fig. 2 we plot

$$\hat{D}_W(n, m) = \frac{\delta \hat{W}(n)}{d_n W_0(n)} - \frac{\delta \hat{W}(m)}{d_m W_0(m)}, \qquad (34)$$

$$\hat{D}_L(n, m) = \frac{\hat{L}(N_t, n)}{c_n L_0(N_t, n)} - \frac{\hat{L}(N_t, m)}{c_m L_0(N_t, m)}. \qquad (35)$$

These quantities vanish when the nth- and mth-order terms are perfectly correlated. Since we measure exact values of $\hat{W}(4)$, $\hat{W}(6)$, $\hat{L}(6, 6)$, $\hat{L}(6, 8)$ in our simulations, we use them for $\hat{W}(m)$ and $\hat{L}(N_t, m)$, while the values measured by the noise method are used for $\hat{W}(n)$ and $\hat{L}(N_t, n)$ in Eqs. (34) and (35). The figure shows that their distribution around zero becomes broader as n becomes larger with fixed m. We also note that the scattering is more suppressed in $\hat{D}_W(n, 6)$ [$\hat{D}_L(n, 8)$] than $\hat{D}_W(n, 4)$ [$\hat{D}_L(n, 6)$] for $n \geq 8$ ($n \geq 10$). This result shows that Eqs. (29) and (30) are superior to Eqs. (23) and (24), respectively, as expected. One also sees that the correlations between the PLT loops survive up to large n, while those between the Wilson loops tend to be blurred more quickly [34].

In Fig. 3, we plot the coefficients in Eq. (26), β_n^*, λ_n^*, as functions of λ in the range relevant for later analyses for various n; as we will see in Sec. IV, the CP is located at $\lambda \simeq 0.0007$. The upper and lower panels plots $\beta_n^* - \beta$ and
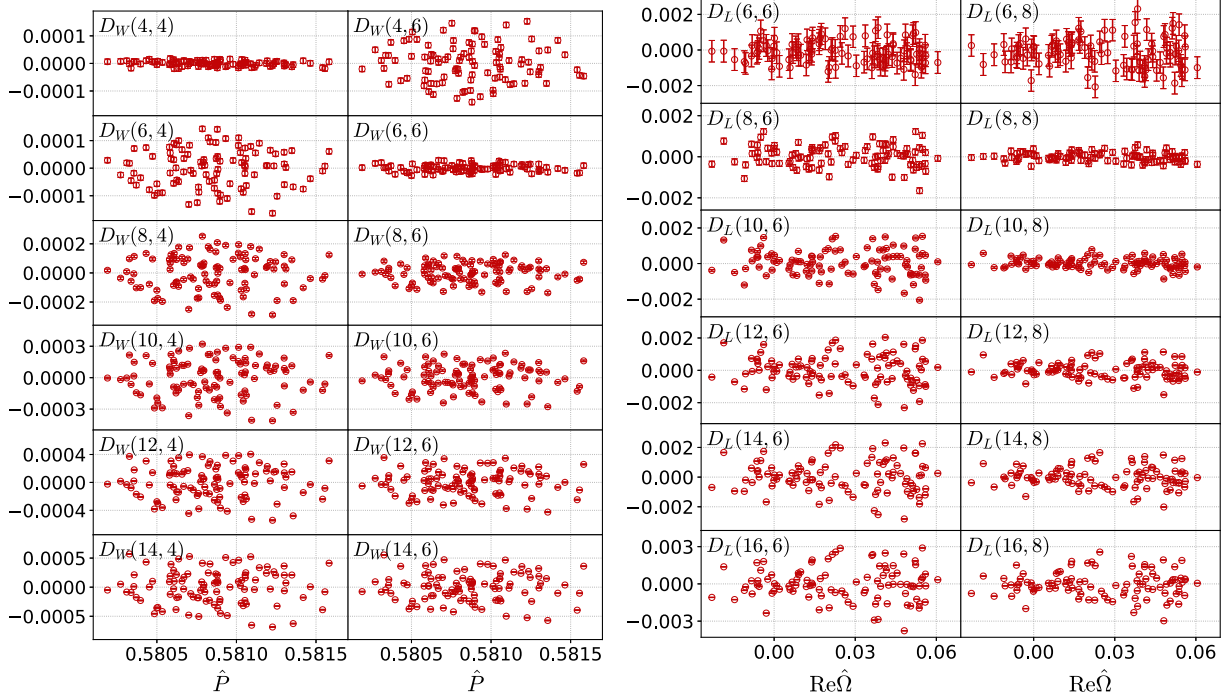

FIG. 2. Scatter plots of $(\hat{D}_W(n, m), \delta \hat{P})$ and $(\hat{D}_L(n, m), \hat{\Omega}_R)$ for various values of n and m. The values measured by the noise method are used for $\hat{W}(n)$ and $\hat{L}(N_t, n)$ in Eqs. (34) and (35), while $\hat{W}(m)$ and $\hat{L}(N_t, m)$ are exactly measured values. Nonzero scatterings in $\hat{D}_W(n, n)$ and $\hat{D}_L(n, n)$ come from the noise method.
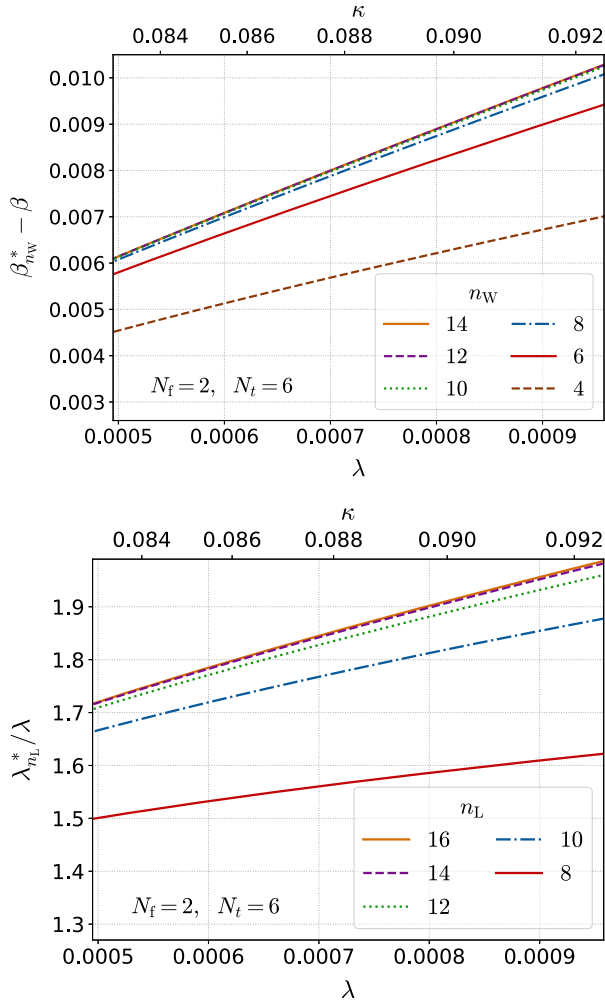
FIG. 3. λ dependence of $\beta^*_{n_W}$ and $\lambda^*_{n_L}$ for various n_W and n_L for $N_f = 2$. The top scale shows the value of κ.

λ^*_n/λ. Notice that these quantities represent the magnitude of the quark contributions to the action at the nth order provided the validity of Eqs. (23) and (24). The figure shows that the coefficients almost converge around $n_W = 10$ and $n_L = 14$, indicating the convergence of the HPE. These results agree with the case of free fermions discussed in Appendix A 1.

Applicability of Eq. (31) may become less justified with large n_W and n_L. However, the rapid convergence of the HPE shown in Fig. 3 indicates that the contribution of the higher-order terms is more suppressed. From Fig. 2, the correlations (29) and (30) hold well until $n_W = 10$ and $n_L = 14$ where the contribution of higher order terms is well negligible in Fig. 3. Therefore, to a good approximation Eq. (31) can be regarded as the action that includes all orders of the HPE near the CP in the heavy-quark region. In the following, we employ Eq. (31) with

$$(n_W, n_L) = (10, 14), \tag{36}$$

for numerical analyses, whereas the use of yet larger n_W and n_L hardly changes the following results.

III. NUMERICAL SETUP FOR BINDER-CUMULANT ANALYSIS

We generate gauge configurations with the action $S_{g+\mathrm{LO}}$ using the method proposed in Ref. [31]. In our previous study at $N_t = 4$, it was found that this method enables high-precision measurements of observables around the CP in the heavy-quark region thanks to efficient Monte-Carlo updates avoiding the overlapping problem in reweighting [31]. As we will see below, the method works well also at $N_t = 6$.

In the present study, we perform the numerical analyses with $N_t = 6$, while the spatial lattice size N_s^3 is varied in the range of the aspect ratio $6 \leq LT = N_s/N_t \leq 18$. For each LT, gauge configurations are generated for $S_{g+\mathrm{LO}}$ at 4–6 sets of (β^*, λ) given in Table II. The value of β^* for each λ is chosen to be close to the transition point at the LO.

The gauge configurations are updated by the pseudo-heat-bath (PHB) and over-relaxation (OR) algorithms [31]. Each PHB step is followed by five OR steps. We measure observables for every 5 set of the PHB + OR updates for $LT \leq 10$. The separation is enlarged to 20 (40) sets for $LT = 12$, 15 ($LT = 18$). We have performed 10^6 measurements at each (β^*, λ) for $8 \leq LT \leq 12$, while the number of measurements is 5×10^5 for $LT = 6$, 7 and 15×10^5 (8×10^5) for $LT = 15$ ($LT = 18$).

Near a first-order phase transition, the autocorrelation length in the Monte-Carlo time tends to be large due to the suppression of the flippings between metastable states. This problem becomes more serious on larger lattices, as well as for smaller λ where the first-order transition is stronger. To see the rate of flippings in the Monte-Carlo time, we show in Fig. 4 the Monte-Carlo history of $\hat{\Omega}_R$ at the smallest λ for $LT = 10$ (top), 15 (middle), and 18 (bottom). The horizontal axis is the Monte-Carlo time in

TABLE II. Simulation parameters β^* and λ. The circles in the right columns denote the values of LT at which the simulations are performed at the parameters in the left columns.

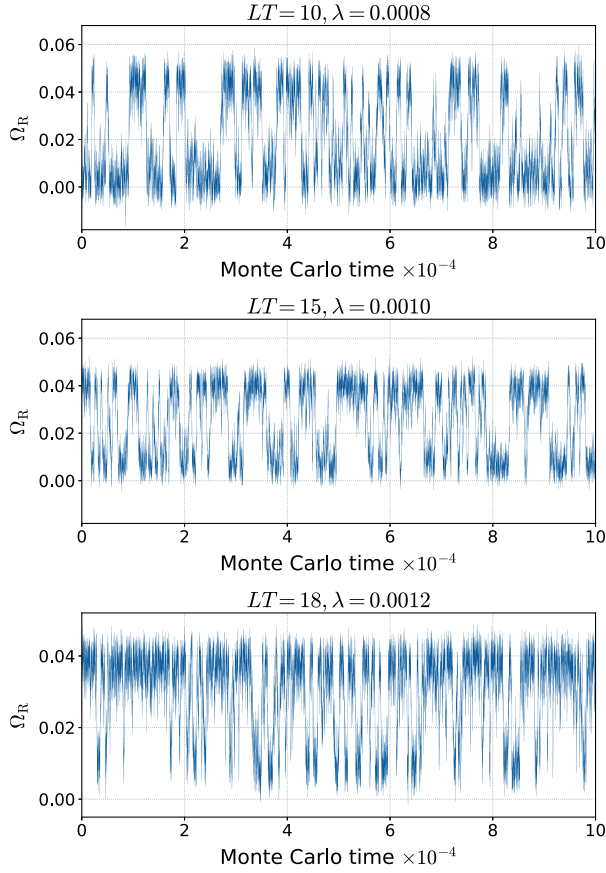|		LT							
λ	β^*	6	7	8	9	10	12	15	18
0.0008	5.8918	○	○	○	○	○			
0.0010	5.8911	○	○	○	○	○	○	○	
0.0012	5.8905	○	○	○	○	○	○	○	○
0.0013	5.8901								○
0.0014	5.8899	○	○	○	○	○	○	○	
0.0014	5.8897								○
0.0015	5.8894								○
0.0016	5.8892	○	○	○	○	○	○	○	
0.0018	5.8886	○	○	○	○	○	○		

FIG. 4. Monte-Carlo time history of $\hat{\Omega}_R$ for $LT = 10, 15, 18$ at the smallest λ in the simulations. The horizontal axis is the Monte-Carlo time in the unit of measurement. The time history for 10^5 measurements is shown for visibility.

the unit of measurement and the figure shows 10^5 measurements among the total ones for visibility. From the figure, one sees that the flipping occurs frequently within the Monte-Carlo time shown in the figure. The autocorrelation lengths of these histories are within 400–800. Since the autocorrelation is moderate even on the largest LT, we do not employ additional Monte-Carlo techniques for its reduction, such as the parallel tempering method [36–38].

To estimate the statistical errors of observables, we use the jackknife analysis with the bin size 25,000, unless otherwise stated. This bin size is significantly larger than the autocorrelation length and large enough to eliminate its effect. In fact, we have checked that statistical errors do not have a clear dependence on the bin size within the interval 10,000–40,000.

On each set of simulation parameters, (β^*, λ), we measure $\hat{P}$, $\hat{P}_6$, $\hat{\Omega}$, $\hat{\Omega}_{N_t+2}$, and other observables on every measurement. From these results, we calculate observables at a physical parameter $(\beta_{\mathrm{ph}}, \lambda_{\mathrm{ph}})$ for the action (31) by reweighting, where both the effects of the parameter shift $(\beta^*, \lambda) \rightarrow (\beta_{\mathrm{ph}}, \lambda_{\mathrm{ph}})$ and the higher-order terms in the HPE

are taken into account. The numerical results thus obtained from individual simulation parameters are averaged over to obtain the final result for each LT.

IV. BINDER CUMULANT

In this section, we perform the numerical analysis of the Binder cumulant of $\hat{\Omega}_R$ near the CP of heavy-quark QCD. In the following, we set $N_f = 2$ unless otherwise stated.

A. FSS of Binder cumulant

The Binder cumulant [33] of $\hat{\Omega}_R$ is defined by

$$B_4 = \frac{\langle \hat{\Omega}_R^4 \rangle_c + 3}{\langle \hat{\Omega}_R^2 \rangle_c^2}, \tag{37}$$

where $\langle \hat{\Omega}_R^n \rangle_c$ is the nth-order cumulant of $\hat{\Omega}_R$.

The CP in heavy-quark QCD is believed to belong to the $Z(2)$ universality class, to which the CP in the three-dimensional Ising model also belongs. If $\hat{\Omega}_R$ corresponds to the magnetization in the Ising model, from the FSS argument it is shown that the minimum of B_4 with the variation of β with fixed λ behaves as

$$B_4(\lambda, LT) = b_4 + c(\lambda - \lambda_c)(LT)^{1/\nu}, \tag{38}$$

near the CP, where the higher-order terms of $\lambda - \lambda_c$ and $1/LT$ are neglected. The CP exists at $\lambda = \lambda_c$, at which $B_4(\lambda, LT)$ with different LT cross at the universal value b_4. In the $Z(2)$ universality class, the values of b_4 and ν are [39]

$$b_4 = 1.604, \qquad \nu = 0.630, \tag{39}$$

whereas the values of λ_c and c are not constrained by the universality.

When $\hat{\Omega}_R$ is not solely given by the magnetization but corresponds to a linear combination of the magnetic- and energylike observables in the Ising model, Eq. (39) is modified as [23,30]

$$B_4(\lambda, LT) = (b_4 + c(\lambda - \lambda_c)(LT)^{1/\nu})(1 + d(LT)^Y), \tag{40}$$

with

$$Y = -0.894, \tag{41}$$

in the $Z(2)$ universality class [39]. In this case, $B_4(\lambda, LT)$ with different LT no longer cross at a point.

B. Numerical results

The use of the minimum value of B_4 in the above argument is motivated by the observation that B_4 takes the minimum at the transition point $\beta = \beta_{\mathrm{tr}}(\lambda)$, which corresponds to the vanishing external magnetic field in the Ising
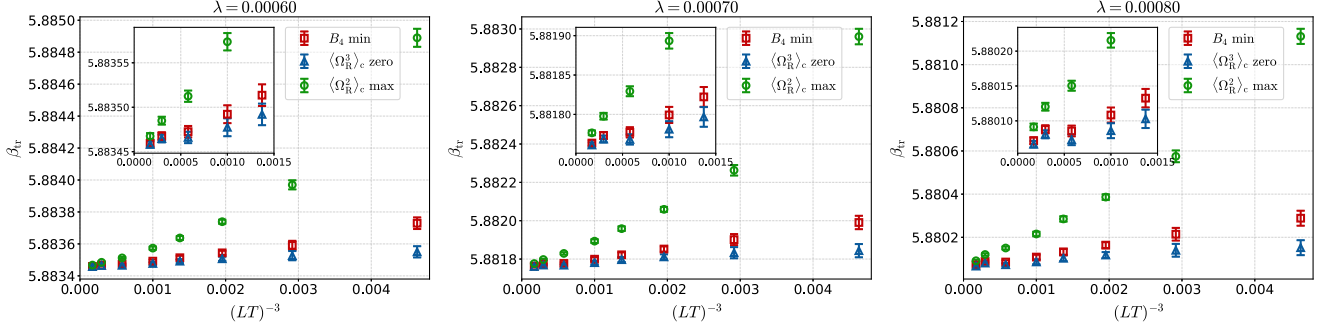
FIG. 5. Transition point $\beta_{\rm tr}(\lambda)$ determined by (i) minimum of B_4, (ii) zero of $\langle\Omega_{\rm R}^3\rangle_c$, and (iii) maximum of $\langle\Omega_{\rm R}^2\rangle_c$, as a function of $(LT)^{-3}$ for $\lambda = 0.0006$, 0.0007, and 0.0008.

model, for a given λ. Alternatively, $\beta_{\rm tr}(\lambda)$ may also be defined through [31,40]

   (i) Maximum of $\langle\Omega_{\rm R}^2\rangle_c$,
   (ii) Zero of $\langle\Omega_{\rm R}^3\rangle_c$.

To check the consistency of these three definitions of $\beta_{\rm tr}(\lambda)$, in Fig. 5 we plot $\beta_{\rm tr}(\lambda)$ obtained by each definition for $\lambda = 0.0006$ (left), 0.0007 (middle), and 0.0008 (right) as functions of $(LT)^{-3}$. The figure shows that all the definitions for $\beta_{\rm tr}(\lambda)$ converge to the same value in the $LT \to \infty$ limit. Among them, the definition through

$\langle\Omega_{\rm R}^2\rangle_c$ has the strongest dependence on LT, while the dependence is milder in the other definitions. In Fig. 6, we show $\beta_{\rm tr}(\lambda)$ obtained from the minimum of B_4 at $LT = 15$ on the β-λ and β-κ planes. The statistical errors are smaller than the thickness of the line.

In Fig. 7, we show the λ dependence of the minimum of B_4 obtained on various LT. The lower panel is an enlargement of the upper. Statistical errors are shown by

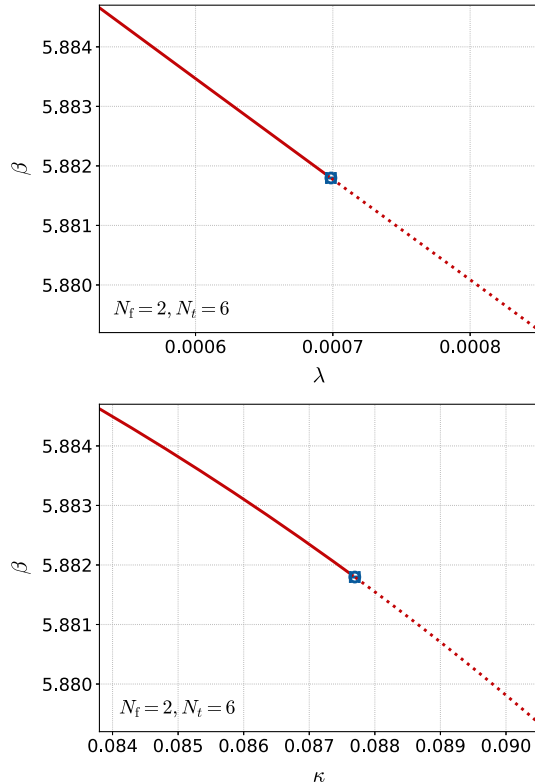FIG. 6. Transition line $\beta_{\rm tr}(\lambda)$ as a function of λ (upper) and κ (lower) obtained from the minimum of B_4 at $LT = 15$. The CP determined by the fit with Eq. (40) is shown by the circle marker. The solid and dashed lines show the first-order transition and crossover. Errors of the line are smaller than the thickness.
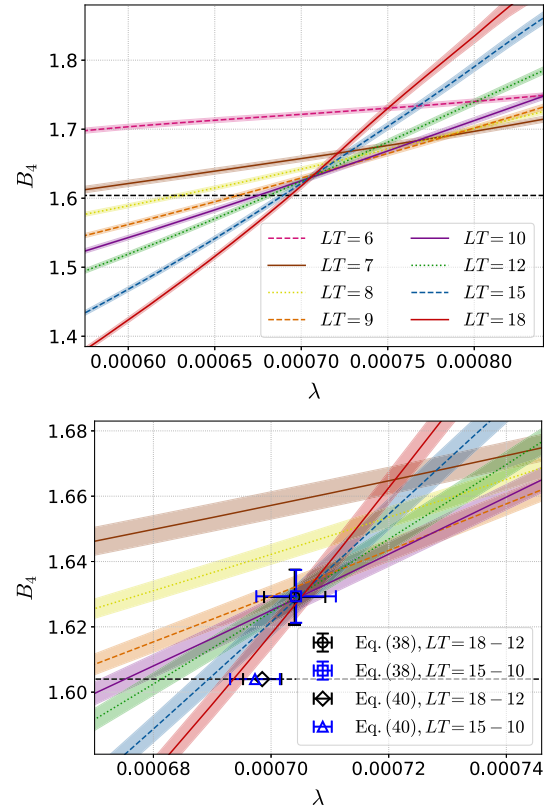

FIG. 7. λ dependence of the minimum of B_4 obtained at various LT. The lower panel is an enlargement of the upper around the crossing point. The circle (square) symbol shows the fit result of the crossing point based on Eq. (38) with $LT \geq 12$ ($LT \geq 10$). The diamond and triangle symbols at $B_4 = b_4$ denote the fit results based on Eq. (40).

the shaded band. To obtain the statistical errors in the jackknife analysis, we measure the minimum value of B_4 on each jackknife sample and use them for the error estimate, i.e., the minimum β value fluctuates sample by sample. The value of B_4 at the CP in the $LT \to \infty$ limit, $b_4 = 1.604$, in Eq. (39) is indicated by the black-dashed lines.

Figure 7 shows that the results for different LT cross around $\lambda = 0.0007$, while the results at smaller LT deviate from this trend; a clear deviation from the crossing point is visible even at $LT = 8$ in the lower panel. Comparing this result to the one on the coarser lattice at $N_t = 4$ [31], one finds that the deviation from the crossing at $N_t = 6$ is more prominent at the same LT. This suggests that the violation of the FSS is more significant, and/or the effect of the mixing of energy-like observable in $\hat{\Omega}_R$ described by Eq. (40) is stronger, on finer lattices.

C. Fit analysis

To determine the location of the CP and the critical exponent ν, we perform the fit analyses of the lattice data based on Eqs. (38) and (40).

First, we perform the four-parameter fit with Eq. (38), where b_4, c, λ_c, ν are the fitting parameters. For the data points to be fitted, we use B_4 at two values of λ, λ_1 and λ_2, for various combinations of LT, where the values of λ_1 and λ_2 are varied within the range $0.00067 \le \lambda_1 \le 0.00069$ and $0.00071 \le \lambda_2 \le 0.00073$ to estimate the systematic uncertainty associated to their choices. The values of B_4 at different λ's are correlated in our analysis because their measurements are performed on the same gauge configurations through reweighting. We take the correlations into account by the correlated fits.

The results of the fits for b_4, λ_c, ν are summarized in Table III for various combinations of LT, where $(\lambda_1, \lambda_2) = (0.00069, 0.00071)$ is employed for the central values. The first and second errors show the statistical and systematic errors, where the latter is estimated from the variations of (λ_1, λ_2), which is well suppressed compared to the statistical error. The results for $LT = (18, 15, 12)$ and $LT = (15, 12, 10)$ are shown in the lower panel of Fig. 7 by the circle and square symbols with the double errors.

The result in Table III shows that the value of the critical exponent ν is consistent with Eq. (39). However, b_4 has more than 2σ deviation from the $Z(2)$ value in Eq. (39) even for the fit with $LT \ge 12$.

To investigate the possible mixing effects of energy-like observable to this result, we next perform the fits based on Eq. (40). However, we found that the six-parameter fit, where b_4, c, λ_c, ν, d, Y are the fitting parameters, is unstable with many local minima of χ^2. We thus fixed b_4, ν, Y to the $Z(2)$ values in Eqs. (39) and (41) and performed the three parameter fit to determine c, λ_c, and d. The results for λ_c for various combinations of LT are shown in Table IV, where

TABLE III. Results of the four-parameter fit based on Eq. (38) for various combinations of LT. The first and second errors are the statistical and systematic ones, respectively, where the latter is estimated from the choices of λ values. The last column shows χ^2/dof of each fit.

LT	b_4	$\lambda_c \times 10^4$	ν	χ^2/dof
18, 15, 12	1.6297(84)(6)	7.048(52)(8)	0.627(19)(5)	0.40
15, 12, 10	1.6294(81)(4)	7.046(68)(4)	0.626(17)(1)	0.35
18–10	1.6295(55)(5)	7.047(38)(3)	0.621(11)(3)	0.23
18–9	1.6331(41)(4)	7.061(32)(7)	0.616(87)(2)	0.47
18–8	1.6418(32)(4)	7.120(27)(8)	0.616(87)(2)	3.95

the meaning of errors is the same as Table III while the central value is set to $(\lambda_1, \lambda_2) = (0.00067, 0.00071)$. The table shows that the fit works well with reasonable χ^2/dof when $LT \ge 10$. The results for $LT = (18, 15, 12)$ and $LT = (15, 12, 10)$ are indicated in the lower panel of Fig. 7 by the diamond and triangle symbols at $B_4 = b_4$ with horizontal error bars. The result for $LT = (18, 15, 12)$ is also shown in Fig. 6 by the circle symbol.

D. Violation of the FSS

Tables III and IV show that χ^2/dof becomes unacceptably large when the numerical results for smaller LT are included. This result indicates that the violation of the FSS shows up for $LT \le 8$ in our data, presumably because the nonsingular contribution to the free energy is not well suppressed there. Compared to Ref. [31], the nonsingular contribution seems to be amplified at the same LT on the finer lattice.

To understand the origin of the violation of the FSS at small LT, we show in Fig. 8 the distribution of $\hat{\Omega}$ on the complex plane at $(\beta, \lambda) = (5.8817, 0.0007)$, the parameter close to the CP, by the color-contour map for $LT = 6, 10, 15$. From the left panel, one finds that the distribution has a triangular shape at $LT = 6$, with distributions extending toward large $|\mathrm{Im}\hat{\Omega}|$ around $\mathrm{Re}\hat{\Omega} = 0$. This behavior is clearly attributed to the remnant of the $Z(3)$ center symmetry at $\lambda = 0$. As a result, the two peaks of the distribution are clearly asymmetric.

In the $Z(2)$ universality class, on the other hand, the scaling function has the rigorous $Z(2)$ symmetry; the magnetization is symmetric against the change of the sign in the Ising model. However, the breaking of this symmetry

TABLE IV. Results of the three-parameter fit based on Eq. (40) for various combinations of LT.

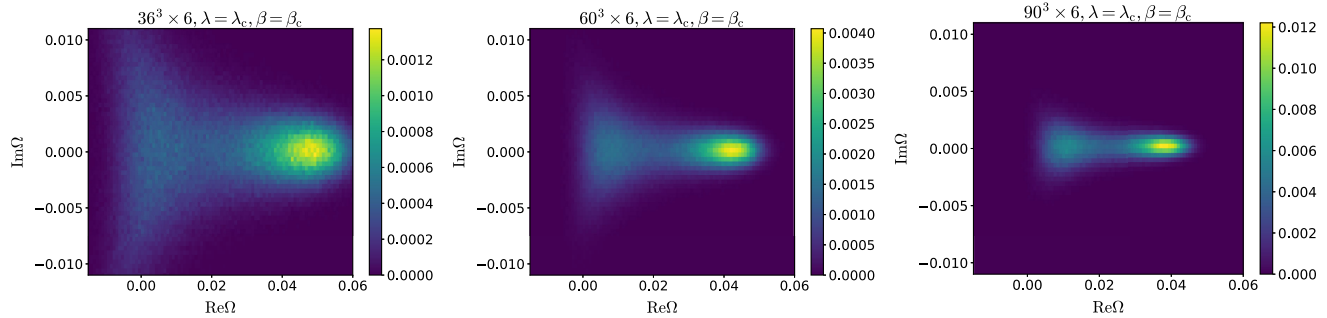| LT	$\lambda_c \times 10^4$	χ^2/dof
18, 15, 12	6.986(32)(9)	0.51
15, 12, 10	6.973(42)(5)	0.83
18–10	6.984(25)(8)	1.07
18–9	6.998(21)(5)	4.23
18–8	7.035(19)(3)	36.4

FIG. 8. Two-dimensional histogram of $\hat{\Omega}$ on the complex plane at the critical point at $LT = 6, 10, 15$.

is manifest in the left panel of Fig. 8, indicating the violation of the scaling behavior at $LT = 6$. While the distribution approaches a symmetric one as LT becomes larger, such violation is visible even on the right panel for $LT = 15$.

The stronger violation of the FSS at $N_t = 6$ than $N_t = 4$ may be related to the strength of the first-order phase transition in SU(3) Yang-Mills (YM) theory corresponding to $\lambda = 0$. It is known that the latent heat in $SU(3)$ YM theory is large at $N_t = 4$ owing to the lattice artifact [41,42]. The large latent heat implies that a stronger external field is necessary to make the transition crossover. As a result, the CP is located at larger λ at $N_t = 4$, where the influence of the original $Z(3)$ symmetry at $\lambda = 0$ is more suppressed.

E. Location of CP: N_f dependence

So far, we have discussed the numerical results for the case of $N_f = 2$. The generalization of these results to other N_f and nondegenerate cases is straightforward as the N_f-dependence of the HPE is explicitly known. In Table V, we summarize the location of the CP for $N_f = 1, 2, 3$. The fitting result using Eq. (40) with $LT = (18, 15, 12)$ is employed as the central value, and the difference from the fit with Eq. (38) is shown by the second error as an estimate of the systematic error due to the fit ansatz.

The location of the CP in the heavy-quark QCD with $N_f = 2$ at $N_t = 6$ has been investigated in Ref. [30] on smaller lattices with the same gauge and quark actions as ours. In this study, the value of κ at the CP is estimated as

$\kappa_c = 0.0877(9)$. This value agrees with the one in Table V, while the error is significantly suppressed in our analysis.

Finally, we may translate the results of the CP in terms of physical observables. In Ref. [30], the pseudoscalar meson mass at zero temperature, m_{PS}, is measured in $N_f = 2$ QCD at several points near the CP at $N_t = 6$ (See, Table III in Ref. [30]). Assuming the absence of β dependence and interpolating κ dependence by the linear interpolation to the value in Table V, we find $m_{PS}/T_c = 18.07(2)\binom{+0}{-2}$ at $\kappa = \kappa_c$ for $N_f = 2$.

V. SUMMARY

In this study, we have performed the Binder-cumulant analysis of the CP in the heavy-quark QCD. We extended our previous analysis at $N_t = 4$ to finer lattices with $N_t = 6$. To see the proper scaling behavior, numerical analyses have been performed on large lattices up to the aspect ratio $LT = 18$. The gauge configurations are generated at the LO action in the HPE, and the effects of higher-order terms are incorporated by the reweighting method. Contributions of the NLO are treated exactly, and yet higher-order terms are incorporated effectively up to virtually infinite order. We have succeeded in realizing high-precision analysis of the Binder cumulant on large spatial volumes while suppressing the truncation errors of the HPE. Precision results for the location of the CP at $N_t = 6$ have been obtained from these results for $N_f = 1, 2, 3$. We also found that the violation of the scaling behavior due to finite volume is more prominent at $N_t = 6$ than our previous study at $N_t = 4$. From the distribution of the Polyakov loop in the complex plane, we argued that the remnant of the $Z(3)$ symmetry at $\lambda = 0$ affects this result.

TABLE V. Parameters of the critical point at $N_t = 6$ for $N_f = 1, 2, 3$. The central values are taken from the fit with Eq. (40). The first errors are statistical, and the second are systematic ones due to the fit ansatz.

N_f	λ_c	κ_c	β_c
1	$0.0006100(27)\binom{+46}{-0}$	$0.09624(7)\binom{+12}{-0}$	$5.88355(5)\binom{+0}{-8}$
2	$0.0006986(32)\binom{+54}{-0}$	$0.08769(7)\binom{+11}{-0}$	$5.88180(5)\binom{+0}{-9}$
3	$0.0007491(36)\binom{+59}{-0}$	$0.08292(7)\binom{+11}{-0}$	$5.88055(6)\binom{+0}{-10}$

APPENDIX: CONVERGENCE OF HPE

In this appendix, we discuss the convergence of the HPE.

1. HPE for free-fermion system

In this subsection, we study the magnitudes of higher order terms of the HPE for the free lattice fermion, which is obtained by substituting $U_{x,\mu} = 1$ into Eq. (3). As discussed in Ref. [34], in this case one can calculate the values of $\hat{W}(n)$ and $\hat{L}(N_t, n)$ analytically, which are denoted by $W_0(n)$ and $L_0(N_t, n)$ in the text.

For the free Wilson fermions, the hopping term (5) is given by [34]

$$b_{xy} = \sum_{\mu=1}^{4} [(1 - \gamma_\mu)\delta_{y,x+\hat{\mu}} + (1 + \gamma_\mu)\delta_{y,x-\hat{\mu}}], \quad (A1)$$

where the Dirac-spinor and color indices are suppressed for notational simplicity. To calculate $W_0(n)$, one may consider infinitely large lattice and Fourier transform the spatial coordinates of Eq. (A1). This procedure leads to

$$W_0(n) = -\frac{1}{n} \text{Tr}[b^n]$$
$$= -\frac{N_c}{n} \int_0^{2\pi} \frac{d^4\varphi}{(2\pi)^4} \text{tr}[\tilde{b}(\varphi)^n], \quad (A2)$$

with

$$\tilde{b}(\varphi) = \tilde{b}(\varphi_1, \varphi_2, \varphi_3, \varphi_4)$$
$$= \sum_{\mu=1}^{4} [(1 - \gamma_\mu)e^{i\varphi_\mu} + (1 + \gamma_\mu)e^{-i\varphi_\mu}]. \quad (A3)$$

Notice that the PLT loops do not contribute to Eq. (A3) since both N_s and N_t are taken to be infinite.

To calculate $L_0(N_t, n)$ we perform the same procedure on the lattice of size $N_s^3 \times N_t$, which leads to

$$W_0(n) + L_0(N_t, n)$$
$$= -\frac{N_c}{N_{\text{site}}n} \sum_{k_1,k_2,k_3=1}^{N_s} \sum_{k_4=1}^{N_t} \text{tr}\left[\tilde{b}\left(\frac{2\pi k_1}{N_s}, \frac{2\pi k_2}{N_s}, \frac{2\pi k_3}{N_s}, \frac{2\pi k_4}{N_t}\right)\right].$$
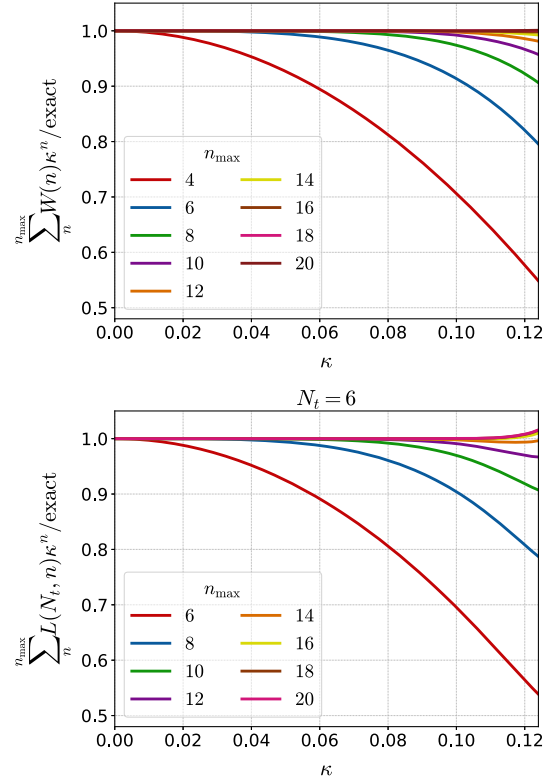$$(A4)$$

FIG. 9. Convergence of the HPE in the weak-coupling limit. The upper (lower) panel shows the contributions of the Wilson (PLT) loops up to nth order to the action S normalized by the exact value.

Then, substituting Eq. (A2) from Eq. (A4) gives $L_0(N_t, n)$. Note that Eq. (A4) is equivalent to Eq. (A2) for $n < N_s$ and $n < N_t$.

For the free-quark system, the quark determinant is given by

$$-\ln\det M = \sum_{n}^{\infty} W_0(n)\kappa^n + \sum_{n}^{\infty} L_0(N_t, n)\kappa^n. \quad (A5)$$

To see the truncation error of the HPE in Eq. (A5), in Fig. 9 we show

$$\sum_{n}^{n_{\text{max}}} W_0(n)\kappa^n, \qquad \sum_{n}^{n_{\text{max}}} L_0(N_t, n), \quad (A6)$$

normalized by the exact value for various n_{max}. In the lower panel, we show the case of $N_t = 6$. From the figure, one sees that Eq. (A6) approaches the exact value as n_{max} becomes larger. As discussed in Sec. IV, the value of κ at the critical point is $\kappa_c = 0.0877$. At this κ, the HPE at NLO, i.e. $n_{\text{max}} = 6$ and 8 for the Wilson and PLT loops, respectively, is already beyond 95% of the exact one. This result suggests that the analysis at NLO gives a good approximation around the CP at $N_t = 6$. The inclusion of

one more higher-order contribution gives an almost perfect approximation.

As discussed in Ref. [34], the convergence of the HPE in the interacting systems is faster than the free-fermion case, since nonunit link variables $U_{x,\mu}$ tends to suppress the higher order terms more significantly.

2. Location of the *CP* in heavy-quark QCD

In Sec. II C, we introduced two methods to effectively incorporate higher-order terms of the HPE with the actions (26) and (31). In this subsection, we compare the numerical results obtained by these methods, as well as the analysis at NLO.

In Fig. 10, we show the transition line as a function of κ and the *CP* determined adopting the actions Eq. (31) (eff[NLO]) and Eq. (26) (eff[LO]), together with the results at NLO, where the transition lines are obtained from the minimum of B_4 at $LT = 15$. The statistical errors are smaller than the thickness of the lines. The CPs are determined by the same analysis as for Table V.

From the figure, we find that, though the NLO calculation should contain about 95% contributions to the action as discussed in the previous subsection, the incorporation of higher-order terms causes a shift of the transition line and the *CP* toward smaller κ compared to the NLO results. Thus, the incorporation of higher-order effects is important for their precise determination. On the other hand, the two alternatives to incorporate higher-order terms, eff[NLO] and eff[LO], give similar results. As discussed in Sec. II D, these results are stable under variations of n_W and n_L. These suggest that the truncation error is well suppressed in these
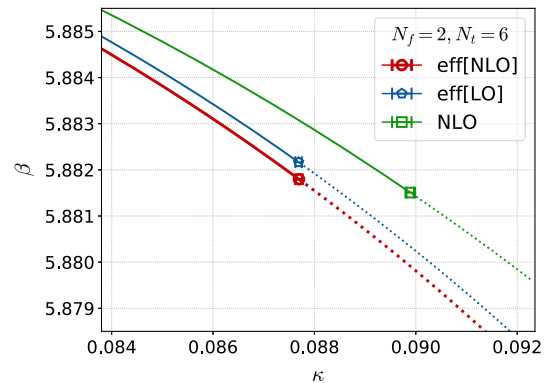

FIG. 10. Transition line and the *CP* obtained for the action Eq. (31) (eff[NLO]), Eq. (26) (eff[LO]), and the action at NLO. The solid and dashed lines show the first-order transition and crossover. The eff[NLO] result is the same as that shown in Fig. 6.

methods. As the eff[NLO] should give the most reliable results among them, we use it in the analyses in the main text.

The convergence of the HPE is eventually violated as the lattice spacing becomes finer with fixed physical quark masses. However, since the difference between eff[NLO] and eff[LO] results is well suppressed in Fig. 10, it is expected that our analysis of the *CP* with eff[NLO] would be well applicable to slightly finer lattices than $N_t = 6$. To go even finer lattices, the analysis of the next-to-next-to-leading order terms in simulations may be necessary to control the truncation errors of the HPE properly.

[1] M. Asakawa and K. Yazaki, Nucl. Phys. **A504**, 668 (1989).

[2] M. Kitazawa, T. Koide, T. Kunihiro, and Y. Nemoto, Prog. Theor. Phys. **108**, 929 (2002); **110**, 185(E) (2003).

[3] M. Asakawa and M. Kitazawa, Prog. Part. Nucl. Phys. **90**, 299 (2016).

[4] M. Bluhm *et al.*, Nucl. Phys. A **1003**, 122016 (2020).

[5] M. Abdallah *et al.* (STAR Collaboration), Phys. Rev. C **104**, 024902 (2021).

[6] M. Abdallah *et al.* (STAR Collaboration), Phys. Rev. C **107**, 024908 (2023).

[7] A. Bazavov *et al.* (HotQCD Collaboration), Phys. Lett. B **795**, 15 (2019).

[8] S. Borsanyi, Z. Fodor, J. N. Guenther, R. Kara, S. D. Katz, P. Parotto, A. Pasztor, C. Ratti, and K. K. Szabo, Phys. Rev. Lett. **125**, 052001 (2020).

[9] M. Scherzer, D. Sexty, and I. O. Stamatescu, Phys. Rev. D **102**, 014515 (2020).

[10] J. N. Guenther, Eur. Phys. J. A **57**, 136 (2021).

[11] M. Fukuma and N. Matsumoto, Prog. Theor. Exp. Phys. **2021**, 023B08 (2021).

[12] L. Dini, P. Hegde, F. Karsch, A. Lahiri, C. Schmidt, and S. Sharma, Phys. Rev. D **105**, 034510 (2022).

[13] P. Dimopoulos, L. Dini, F. Di Renzo, J. Goswami, G. Nicotra, C. Schmidt, S. Singh, K. Zambello, and F. Ziesché, Phys. Rev. D **105**, 034513 (2022).

[14] S. Borsanyi, Z. Fodor, M. Giordano, S. D. Katz, D. Nogradi, A. Pasztor, and C. H. Wong, Phys. Rev. D **105**, L051506 (2022).

[15] Y. Namekawa, K. Kashiwa, H. Matsuda, A. Ohnishi, and H. Takase, Phys. Rev. D **107**, 034509 (2023).

[16] G. Aarts *et al.*, Prog. Part. Nucl. Phys. **133**, 104070 (2023).

[17] T. Yokota, Y. Ito, H. Matsufuru, Y. Namekawa, J. Nishimura, A. Tsuchiya, and S. Tsutsui, J. High Energy Phys. 06 (2023) 061.

[18] D. A. Clarke, P. Dimopoulos, F. Di Renzo, J. Goswami, C. Schmidt, S. Singh, and K. Zambello, arXiv:2405.10196.

[19] R. D. Pisarski and F. Wilczek, Phys. Rev. D **29,** 338 (1984).

[20] O. Philipsen, Symmetry **13,** 2079 (2021).

[21] D. Fujii, A. Iwanaka, M. Kitazawa, and D. Suenaga, arXiv:2404.07899.

[22] H. Saito, S. Ejiri, S. Aoki, K. Kanaya, Y. Nakagawa, H. Ohno, K. Okuno, and T. Umeda, Phys. Rev. D **89,** 034507 (2014).

[23] X.-Y. Jin, Y. Kuramashi, Y. Nakamura, S. Takeda, and A. Ukawa, Phys. Rev. D **88,** 094508 (2013).

[24] S. Ejiri, R. Iwami, and N. Yamada, Phys. Rev. D **93,** 054506 (2016).

[25] A. Bazavov, H. T. Ding, P. Hegde, F. Karsch, E. Laermann, S. Mukherjee, P. Petreczky, and C. Schmidt, Phys. Rev. D **95,** 074505 (2017).

[26] X.-Y. Jin, Y. Kuramashi, Y. Nakamura, S. Takeda, and A. Ukawa, Phys. Rev. D **96,** 034523 (2017).

[27] S. Ejiri, S. Itagaki, R. Iwami, K. Kanaya, M. Kitazawa, A. Kiyohara, M. Shirogane, and T. Umeda (WHOT-QCD Collaboration), Phys. Rev. D **101,** 054505 (2020).

[28] O. Philipsen, Proc. Sci., LATTICE2019 (**2019**) 273 [arXiv:1912.04827].

[29] Y. Kuramashi, Y. Nakamura, H. Ohno, and S. Takeda, Phys. Rev. D **101,** 054509 (2020).

[30] F. Cuteri, O. Philipsen, A. Schön, and A. Sciarra, Phys. Rev. D **103,** 014513 (2021).

[31] A. Kiyohara, M. Kitazawa, S. Ejiri, and K. Kanaya, Phys. Rev. D **104,** 114509 (2021).

[32] Y. Zhang, Y. Aoki, S. Hashimoto, I. Kanamori, T. Kaneko, and Y. Nakamura, Proc. Sci., LATTICE2022 (**2023**) 197 [arXiv:2212.10021].

[33] K. Binder, Z. Phys. B **43,** 119 (1981).

[34] N. Wakabayashi, S. Ejiri, K. Kanaya, and M. Kitazawa, Prog. Theor. Exp. Phys. **2022,** 033B05 (2022).

[35] H. J. Rothe, *Lattice Gauge Theories: An Introduction* (World Scientific, Singapore, 1992), Vol. 43.

[36] B. Joo, B. Pendleton, S. M. Pickles, Z. Sroczynski, A. C. Irving, and J. C. Sexton (UKQCD Collaboration), Phys. Rev. D **59,** 114501 (1999).

[37] G. Burgio, M. Fuhrmann, W. Kerler, and M. Muller-Preussker, Phys. Rev. D **75,** 014504 (2007).

[38] S. Borsanyi, K. R., Z. Fodor, D. A. Godzieba, P. Parotto, and D. Sexty, Phys. Rev. D **105,** 074513 (2022).

[39] A. Pelissetto and E. Vicari, Phys. Rep. **368,** 549 (2002).

[40] S. Borsanyi, Z. Fodor, J. N. Guenther, R. Kara, P. Parotto, A. Pasztor, and D. Sexty, Proc. Sci., LATTICE2021 (**2022**) 496 [arXiv:2112.04192].

[41] M. Shirogane, S. Ejiri, R. Iwami, K. Kanaya, and M. Kitazawa, Phys. Rev. D **94,** 014506 (2016).

[42] M. Shirogane, S. Ejiri, R. Iwami, K. Kanaya, M. Kitazawa, H. Suzuki, Y. Taniguchi, and T. Umeda (WHOT-QCD Collaboration), Prog. Theor. Exp. Phys. **2021,** 013B08 (2021).